J Therm Spray Tech (2021) 30:1380–1392
https://doi.org/10.1007/s11666-021-01202-1

PEER REVIEWED

Effects of Particle Size on the Microstructure and Mechanical Properties of HVAF-Sprayed Al-Based Quasicrystalline Coatings

Meng Xiao[1,2] · Xiaoqing Liu[1,2] · Sihui Zeng[1,2] · Zhigang Zheng[1,2] · Gang Wang[1,2] · Zhaoguo Qiu[1,2] · Min Liu[3] · Dechang Zeng[1,2]

Submitted: 7 September 2020 / in revised form: 16 March 2021 / Accepted: 21 March 2021 / Published online: 6 May 2021

Abstract To obtain dense Al-based quasicrystalline (QC) coatings with high content of quasicrystal phase, the QCs were deposited by the high-velocity air fuel spray process with different feedstock powder sizes. The phase composition, microstructure, chemical composition, tribological, and mechanical properties of the coatings were analyzed using x-ray diffraction, scanning electron microscopy, energy-dispersive x-ray spectroscopy, a pin-on-disk wear tester, and a nanohardness tester. The results indicated that smaller particle sizes produced denser structures with lower coating porosities, while the coarser powder helped maintain the desired quasicrystalline phase. In addition, the coatings sprayed with coarser powders exhibited a lower sensitivity to the sliding velocity due to a stronger bonding strength between the splats and a lower oxidation degree. The coating first exhibited abrasive wear coupled with oxidative wear, which was then converted to delamination, abrasive wear, and intensified oxidative wear.

✉ Zhaoguo Qiu
zgqiu@scut.edu.cn

✉ Dechang Zeng
medczeng@scut.edu.cn

Meng Xiao
411869266@qq.com

[1] School of Materials Science and Engineering, South China University of Technology, Guangzhou 510640, China

[2] Zhongshan R&D Center for Materials Surface and Thin Films Technology of the South China University of Technology, Gent Materials Surface Technology (Guangzhou) Co., Ltd, Zhongshan 528437, China

[3] Institute of New Materials, Guangdong Academy of Sciences, Guangzhou 510651, China

Keywords HVAF · particle size · quasicrystalline coatings · wear resistance

Introduction

Quasicrystals (QCs) exhibit unique atomic structures and very unusual physical and transport properties, such as low conductivity with positive thermal coefficient (Ref 1), high hardness and strength, low friction coefficient (Ref 2), high oxidation, and corrosion resistance (Ref 3). However, the applications for large-scale Al-based bulk QC are limited due to their extreme brittleness at ambient temperature (Ref 2). Fortunately, thermal spraying has been reported to be an effective and promising approach to overcome the brittle drawbacks of Al-based QCs (Ref 3, 4). In the high-velocity air fuel (HVAF) spray system, high-temperature supersonic gas stream utilizes the superplastic behavior of the QC materials (Ref 5). In addition, the M3 torch design together with the replacement of combustion-supporting media from pure oxygen into compressed air minimizes microstructural and chemical changes in the feedstock powder (Ref 6, 7). As a result, the designed crystal structure and favorable properties of the feedstock powder material are maintained in the sprayed coating (Ref 6, 8). Thus, the HVAF shows its potential for depositing QC coatings.

The particles may exhibit variable velocities and melting states (Ref 9, 10) based on the coating material properties (material type and particle size) and process parameters (flame temperature and carrier gas velocity) employed, which ultimately produces various morphologies when impacting a substrate. In the development of A1-Cu-Fe coatings for tribological applications, minimal porosity and high fraction of quasicrystal phase are

required. Considerable works have been devoted to understanding the effects of the material properties and process parameters on the microstructure, phase content, and mechanical properties of coatings. Yin et al. (Ref 11) found that finer feedstock sizes improved the particle velocity and temperature as well as the melting extent. Notably, an increased particle velocity may worsen the melting state due to a shorter dwell time in the accelerated nozzle (Ref 12). In the spraying process, a proper combination of surface temperature and in-flight velocity is usually more beneficial for the deposition of droplets. Li et al. (Ref 10) reported that the solid–liquid two-phase droplets (partially melted particle) contributed to the high adhesive strength of the HVAF-sprayed Ni-based coating. In comparison, the splats with disk-like shapes or near disk-like morphology were conducive to reducing or eliminating the defects of the as-sprayed coating and forming a fine lamellar-structured coating (Ref 13). Therefore, it is important to control the particle size to adjust the in-flight behavior (particle temperature and velocity) of the droplet and its deformation degree. However, due to the complex solidification path when forming Al-Cu-Fe quasicrystals, the overheating of finer particles may change the chemical composition. For example, fine Al-Cu-Fe particles show a substantial loss of Al, thus shifting the coating composition away from the single-phase QC region of the Al-Cu-Fe phase diagram (Ref 8). Moreover, the low thermal conductivity of the QC phase increases the opportunity to overheat and partially vaporize the Al element in the spraying process (Ref 8). By contrast, it is equally necessary to have coating parameters that do not change the composition of the powder if a uniform coating microstructure is desired. Therefore, under identical spraying conditions, a strict control of the particle size and its distribution are of great importance when modifying the melting state to obtain a fine lamellar-structured coating with a high QC phase content.

In this work, the effect of the starting particle size and its distribution on the microstructure, phase constitutions, and mechanical properties of QC coatings was investigated. In addition, their wear mechanisms were also discussed.

Experimental Procedure

Materials and Specimen Preparation

$Al_{65}Cu_{20}Fe_{10}Cr_5$ (at.%) quasicrystal powders were obtained by high-pressure gas atomization in an argon atmosphere. The as-atomized powders with various size distributions were used for HVAF spraying, and the powder size was analyzed by a laser diffraction system (Better size 2000LD). Feedstocks with the median sizes (D_{50}) of 9.48, 22.48, 38.47, and 29.65 μm were designated as P1, P2, P3, and P4, respectively. The corresponding coatings were denoted as C1, C2, C3, and C4, respectively. Additionally, particles with D_{50} = 65.59 μm were termed P5 in the single splat deposition process. The size distributions of all the powders are listed in Table 1. Before coating fabrication, the ASTM 1045 steel was mechanically polished and then cleaned by ethanol. Afterward, the grit-blasted process was conducted to provide a fresh and rough surface for good bonding strength. The experimental schematic diagram is shown in Fig. 1. First, the coatings were fabricated by the HVAF thermal spray system (Unique Coat Technologies M3^{TM} Supersonic HVAF Spray System), where powders with various size distributions were accelerated in a de Laval nozzle (2L2). An air-jet cooling system was also utilized at the back of the substrate plates to inhibit the thermal-induced impacts both during and after the HVAF deposition process. Additionally, the temperature of the substrate was measured after two spraying passes to ensure the substrate temperature was below 100°C; eight passes were completed for each sample. The spraying parameters are listed in Table 2. Second, the effects of the powder size on the coating properties (porosity, hardness, and surface roughness) and droplet spreading behavior were investigated. In addition, the wear resistance and wear mechanisms were also studied. The splats were deposited with P1, P2, P3, and P5 at a torch travel speed of 1000 mm/s under the same spraying parameters.

Characterization of Coatings

The phase structures of powders and coatings were characterized by x-ray diffraction (XRD, Philips X-Pert Pro) with Cu-Ka radiation and focused ion beam (FIB, 450S, FEI)-assisted transmission electron microscopy (TEM, JEM2100F, JEOL, Japan). The morphology of the powders and coatings was observed by scanning electron microscopy (SEM, Nova Nano SEM 430) coupled with energy-dispersive spectroscopy (EDS). The porosity was measured by using Image-Pro Plus 6.0. More than five digital SEM photos with 1000× magnification were analyzed to obtain the statistically averaged values. The microhardness (HVS-1000) was detected on the polished surface under a load of 300 g for 15 s; at least six measurements were completed for each sample. The hardness and elastic modulus of the coatings were tested by a CSM nano-indentation instrument equipped with Berkovich diamond tip with a load of 30 mN and loading rate of 15 mN/min. The eight valid points were used to obtain the average values. Inductively coupled plasma-optical emission spectroscopy (ICP-OES, Agilent 700) was used to determine the Al, Cu, Fe, and Cr contents of the coatings, while the oxygen contents of the

Table 1 Size distributions of $Al_{65}Cu_{20}Fe_{10}Cr_5$ powders

Powders	D_{10}, μm	D_{50}, μm	D_{90}, μm	Specific surface area, m^2/g
P1	5.03	9.48	15.11	0.274
P2	8.98	22.48	34.19	0.130
P3	23.31	38.47	57.69	0.070
P4	12.34	29.65	47.51	0.098
P5	40.23	65.59	82.34	0.042

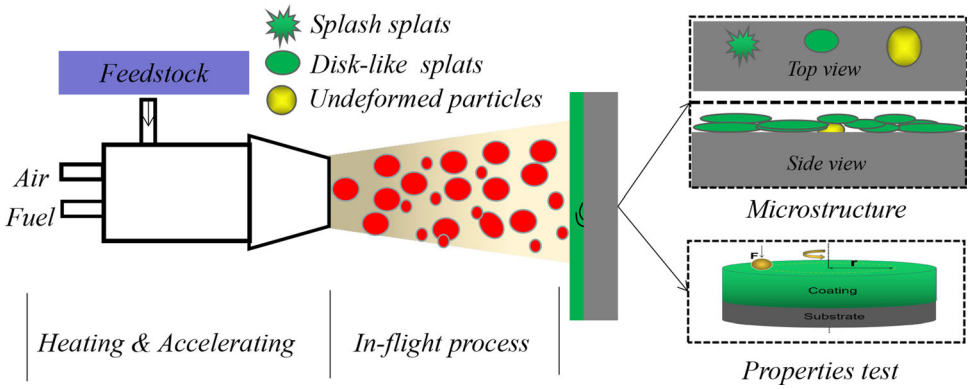

Fig. 1 Schematic diagram of HVAF spraying

Table 2 Spraying parameters

Parameters	Values
Spraying distance, mm	150
Powder feed rate, g min^{-1}	20
Fuel gas pressure, MPa	0.75
Compressed air pressure, MPa	0.82
Carrier gas flow rate, L/min	68
Traverse speed, mm/s	300
Pass spacing, mm	3

powders and coatings were measured using an oxygen–nitrogen analyzer (Leco, ONH836).

The wear resistance of the coatings was measured by the pin-on-disk tester (SFT-2M) at room temperature. Each test was carried out in triplicate. All samples with dimensions of 15 × 15 × 5.5 mm were prepared by a wire cutting machine. Before the friction trial, all samples were wet-ground and then polished to a mirrored finish, cleaned in alcohol, and finally dried in warm air. Alumina with a diameter of 4 mm and mean surface roughness of approximately 70 nm was selected as the grinding ball. The test parameters were as follows: radius of rotation of 3 mm, sliding speed of 0.1–0.2 m/s, applied load of 16 N, and a fixed sliding time of 15 min. A 3D optical measurement system (SMS expert) was used to measure the profile of wear tracks and surface roughness. The wear rate was then calculated using the equation of $Q = V_w\ N^{-1}\ S^{-1}$, where Q is the wear rate in mm^3/Nm, V_w is the wear volume loss, and N and S represent the applied load and the total sliding distance, respectively.

Results and Discussions

Characterization of Feedstock Powders and Coatings

Figure 2 shows four kinds of size distributions and morphologies for the powders. Figure 2(a) indicates that the fine particles (P1) were spherical with certain small satellite powders attached onto them. By contrast, bigger particles (P3) were spherical or near-spherical and exhibited rougher surface (Fig. 2b), while several pores were observed on the cross-sectional morphology of the coarser particles (Fig. 2c). The powder morphology variation was caused by the differences in the cooling rate together with the droplets' collision during preparation (Ref 14, 15). In addition, the pores originated from the entrapped atomizing gas during atomization.

Figure 3 shows the XRD patterns of the $Al_{65}Cu_{20}Fe_{10}Cr_5$ powders and coatings. The results revealed that all the feedstocks and coatings consisted of the same phases, including icosahedral quasicrystalline phase (i-QC phase), τ-AlCu(Fe), and β-Al(Cu,Fe) phases. As powder size increases, the feedstock powder presented a higher β-Al(Cu,Fe) phase content at the expense of the icosahedral phase. Unlike the powder patterns, the major phase in C1 changed into a τ-AlCu(Fe) phase instead of β-Al(Cu,Fe) as compared to the other coatings. The XRD results were employed to qualitatively measure the areas of the i-QC and crystalline phases. The icosahedral phase volume fraction was calculated using the following formula (Ref 16):

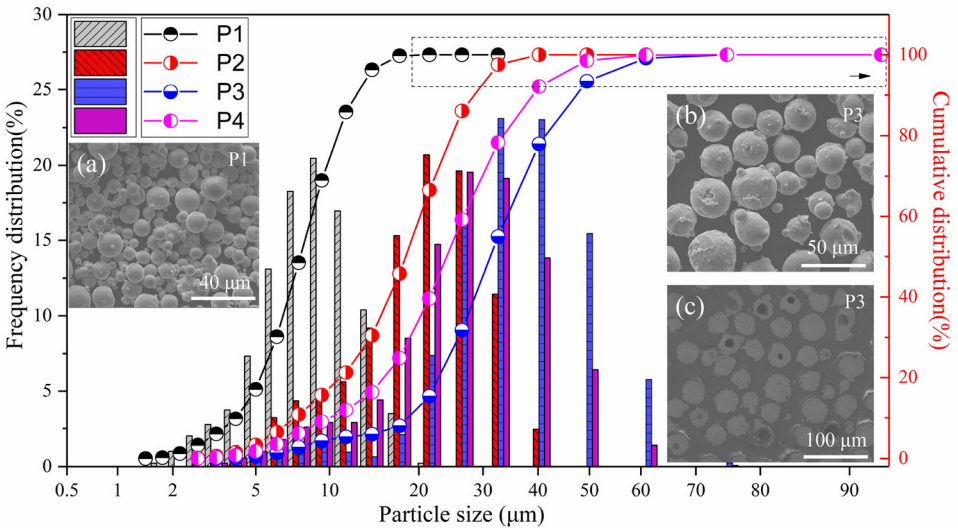

Fig. 2 Particle size distributions of as-atomized powder. The insets show the surface and cross section images of powders: (a) P1, (b) and (c) P3

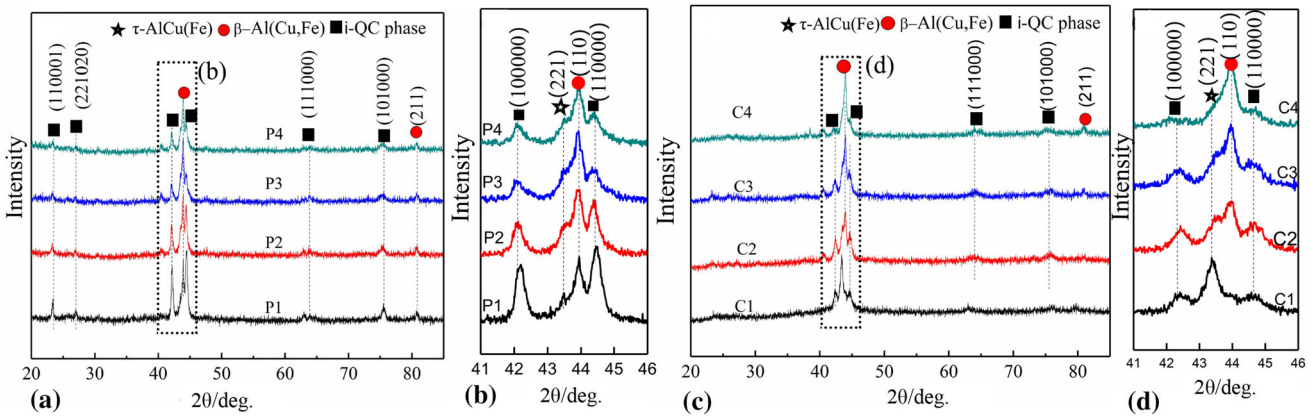

Fig. 3 XRD patterns of the $Al_{65}Cu_{20}Fe_{10}Cr_5$ powders and corresponding coatings: (a) and (b) powders; (c) and (d) coatings

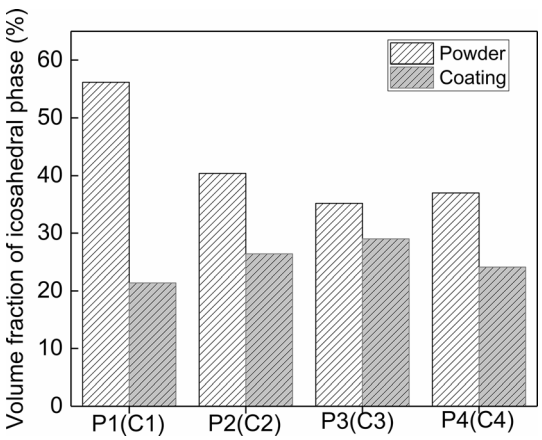

Fig. 4 The volume fraction of icosahedral phase of various powders and coatings

$$V_{\text{ico}} = \frac{A_{\text{ico}}}{A_{\text{ico}} + A_{\text{crys}}} \times 100\%$$

where V_{ico} and A_{crys} are the areas of the icosahedral phase peaks and all crystalline peaks, respectively. Figure 4 presents a comparison between the icosahedral phase contents (V_{ico}) of the coatings and those of the powders. Interestingly, the powder size significantly affected V_{ico} of the powders, which decreased from 56.2% for P1 to 35.2% for P3. In comparison, V_{ico} increased from 21.4% for C1 to 29.0% for C3. A previous study reported that the formation mechanism of the icosahedral phase is significantly dependent upon the cooling rate (Ref 5). The high cooling rate resulted in the formation of a dendritic i-QC phase from the undercooled liquid without the precipitation of the primary τ- and β-phases. For a moderate cooling rate, a peritectic reaction resulted in the formation of the icosahedral phase. In our case, an increase in the powder size likely reduced the cooling rate and consequently led to the formation of the β-phase. Thus, V_{ico} of the powders reached their peak value for P1 and then decreased as the powder size increased. The change in the coating phase assemblage indicated that, at a lower particle size of

D_{50} = 9.48 µm, heat rapidly transferred from the flame to the flight particles, promoting the vaporization of aluminum, which facilitated in the formation of the crystalline phase rather than the QC phase. In addition, the oxidation of the powder increased when the fine QC powders were exposed to the oxidizing atmosphere, which further decreased V_{ico}. As the particle size increased, the flame energy was not high enough to sufficiently melt the powders. Therefore, the coating contained a significant amount of semi-molten particles, such that its i-QC phase content was closer to that of the feedstock powders.

Figure 5 shows the representative bright-field TEM images (a1, a2), HR-TEM image (b), and SAED patterns along the fivefold (c) and twofold (d) axis of the AlCuFeCr coating. The SAED patterns with fivefold symmetries (Fig. 5c) and twofold symmetries (Fig. 5d) confirmed that the quasicrystalline phase was in the i-QC phase.

Figure 6 shows the surface morphology of the as-sprayed $Al_{65}Cu_{20}Fe_{10}Cr_5$ coatings. The solidified splat morphologies were significantly different in the coatings deposited with different powder sizes. The rough surface contained splashed splats, flower-like splats, and/or partially melted splat. The splashed splats and fragmented splats were observed in the C1, C2, and C4 coatings. In comparison, more fragmented splats together with broken solid particles were observed in the C3 coating. Furthermore, the smooth surface of splash splats exhibited several cracks (Fig. 6a2 and d3). The splat with the smooth surface and microcrack was considered a fully molten splat-type, irrespective of its shape (Ref 17). Usually, feedstocks with a certain fraction of fine particles are prone to forming splash splats due to the higher temperature and velocity of the molten droplets (Ref 18). The surface microcracks were induced by the rapid cooling (quenching) of the impinging droplet. In this way, the quenching stresses caused by the thermal stress and bonding constraint strain with the substrate were released. The splash pattern disappeared, and some un-deformed particles were observed on the C3 and C4 coating surfaces as the powder size was increased. These large fragments sharply lowered the particle bonding strength after collision, which also promoted the generation of pores and cracks (Ref 19).

The compositions of all the as-sprayed of coatings are summarized in Table 3. It seems that all the coatings lost

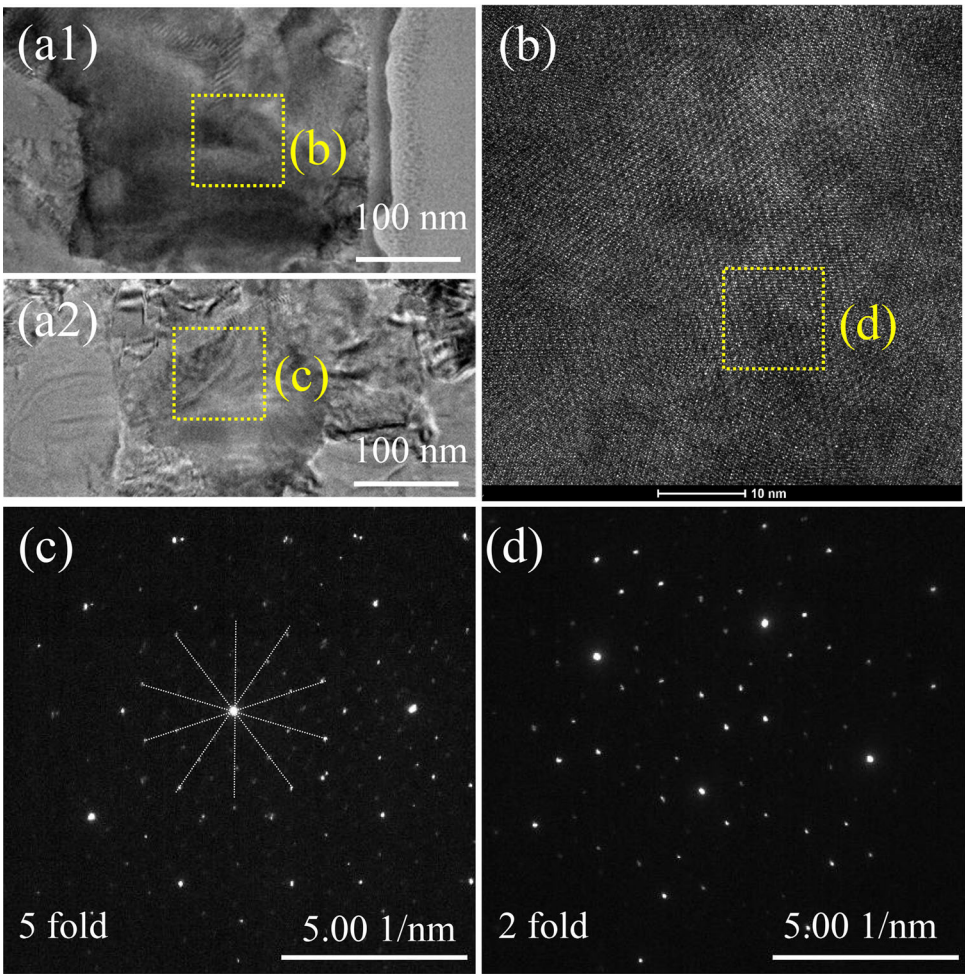

Fig. 5 TEM images of the Al-Cu-Fe–Cr coating: (a1-a2) bright-field TEM images, (b) HR-TEM image of area taken from (a), (c) (d) selected area electron diffraction (SAED) patterns of area (c) and (d) taken along fivefold and twofold axis of QC coating

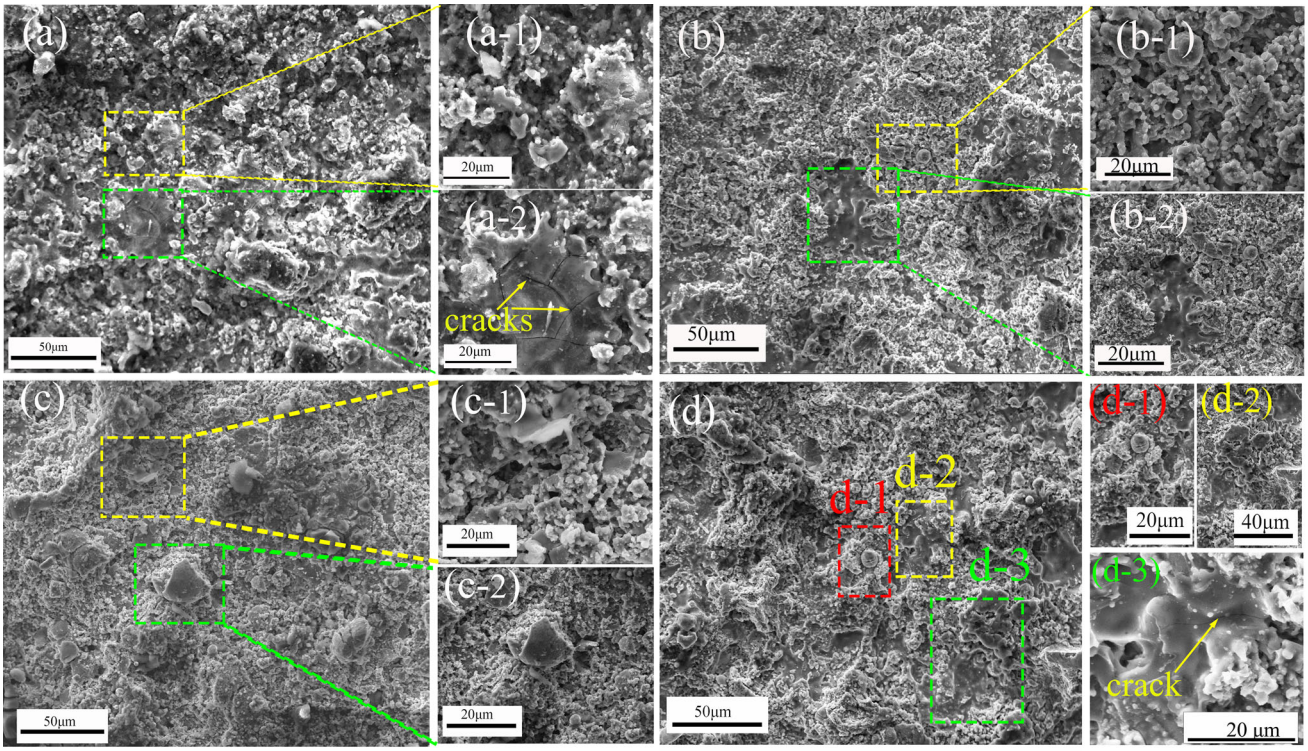

Fig. 6 Surface morphology of the coatings: (a) C1, (b) C2, (c) C3 and (d) C4

Table 3 Chemical constituents of starting powders and coatings (wt.%)

Samples	Compositions, wt.%				
	Al	Cu	Fe	Cr	O
P1-P4	45.6	33.0	14.5	6.8	0.21, 0.12, 0.08, 0.13
C1	40.1	32.3	12.6	6.2	1.7
C2	43.7	32.6	12.7	6.3	0.9
C3	44.6	34.0	12.6	6.5	0.5
C4	44.1	34.6	13.5	6.6	0.8

some Al during spraying, and the amount of oxygen element was inversely proportional to the powder size. Coatings formed as the finer powders lost more Al and also gained more oxygen. A previous study reported that the chemical variations of the formed coatings with different as-atomized powders were due to the initial reactions between the particles and the heat source prior to its deposition onto the substrate (Ref 8). Therefore, the oxygen incorporated into the coating during spraying was likely in the form of Al_2O_3. Considering this fact, the total Al element actually involved in the formation of various intermetallic and QC phases was less than that of reported Al content in Table 3. The oxidation- and evaporation-induced element loss may have moved the composition of the i-QC phase out of the stability field, which resulted in the precipitation of the cubic β-Al(Fe,Cu) phase (CsCl type); finer powders exhibit more serious results.

Figure 7 shows the cross-sectional morphology of C1–C4 coatings. The thickness of coatings was in the range of 164-309 μm. Notably, few pores were found in the C1 and C2 coatings, while several pores were observed inside the C3 and C4 coatings. The porosity of C1–C4 was approximately 1.21, 1.33, 1.45, and 1.02%, respectively. The porosity commonly originates from two aspects due to the stack-based essence of thermal spraying. On the one hand, oxide films generated on the particle surface may reduce the wetting degree with splats, leading to the formation of defects (Ref 20). On the other hand, shrinkage phenomenon may occur for the fully melting droplets during the solidification process (Ref 21). When increasing the powder size, unmelted particles with pores (marked with yellow cubes) were found along the interface of coating and substrate in the C3 and C4 coatings, as shown in Fig. 7(c) and (d). In addition, numerous horizontal cracks (marked with green cubes) were observed next to the unmelted particles, indicating that the large-sized particle impacted by the substrate was in the solid phase state. Figure 7(e) shows the cracks or interlayer regions in the C3 coating. Combined with the EDX line scanning result, relatively severe oxidation was observed in such regions. The unavoidable oxidation of the in-flight particles was easily induced

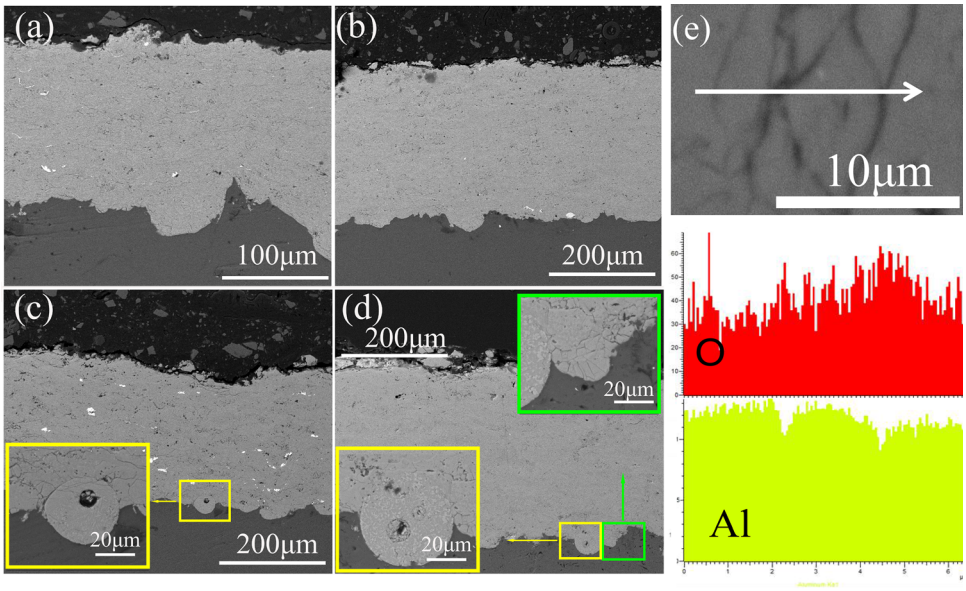

Fig. 7 Cross section morphologies of coatings: (a) C1, (b) C2, (c) C3, (d) C4, the inset is magnified view of unmelted particle; (e) cracks and intersplat region in the coating, and EDX line scanning analysis

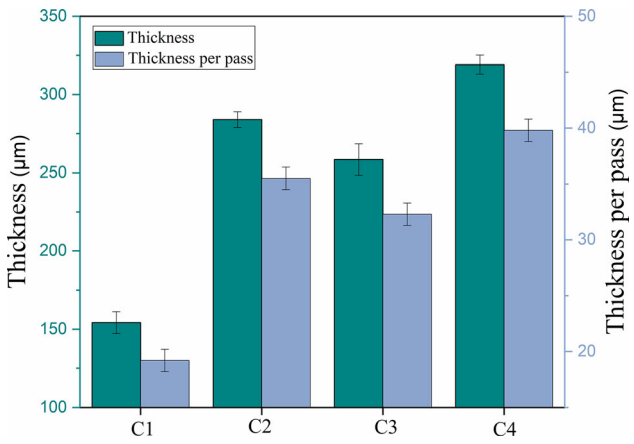

Fig. 8 The thickness and thickness of pass of the coatings

during the deposition process in air. As a result, defect regions were observed, which triggered the formation of cracks, thus increasing the spallation, delamination, and pits and ultimately resulting in severe abrasive wear.

Figure 8 presents the coating thickness and the thickness per pass. The C1–C4 coatings exhibited thicknesses of 154.2, 284.0, 258.5, and 319.1 μm, respectively, as well as thicknesses per pass of 19.3, 35.5, 32.3, and 39.9 μm, respectively. These results indicate that the deposition efficiency of P2–P3 was two- to threefold higher than those of the finer powder (P1), indicating a better melting state (Fig. 6a). According to the surface (Fig. 6) and cross section (Fig. 7) images of the coatings, the fine particles exhibited increased particle temperatures and velocities, thus producing a dense structure. However, the overheated particle also resulted in hypervelocity impact phenomena with noticeable sputtering. Consequently, the deposition efficiency was significantly reduced. As compared to C2 and C4, C3 prepared with a coarse particle size exhibited a lower deposition efficiency due to reduced melting state, as confirmed by Fig. 6(c). Part of the large feedstock may have rebound and eroded the already deposited coating. As a result, the coating thickness and deposition efficiency were slightly reduced.

Mechanical Properties

Porosity and hardness significantly affected the quantification of material properties, including the strength, fatigue limit, and wear resistance (Ref 22). Figure 9 exhibits variations in porosity, microhardness ($HV_{0.3}$), and surface roughness with the size distribution. An increase in the particle size, porosity, and microhardness exhibited the opposite tendency. At a P1 with D_{50} of 9.48 μm, C1 possessed the highest hardness of approximately 683.2 $HV_{0.3}$ and a low porosity of 1.21%. A further increase in the D_{50} at the largest value of 38.47 μm resulted in the highest C3 coating porosity of 1.45% and the lowest C3 coating hardness of 562.5 $HV_{0.3}$. Therefore, an increase in the particle size gradually reduced the deformation degree of the droplets and then generated a loose coating microstructure, which contained numerous pores, partially melted particles, and microcracks. Meanwhile, the C4 coating, which was prepared at the widest particle size range, obtained the lowest porosity of 1.02% due to the peening effect between the large particles and newly deposited coatings, which made the coatings more compact. In addition, the C1, C2, C3, and C4 coating exhibited roughness values (R_a) of 8.86, 5.96, 8.44, and 7.52 μm, respectively. Among them, C1 obtained the maximum

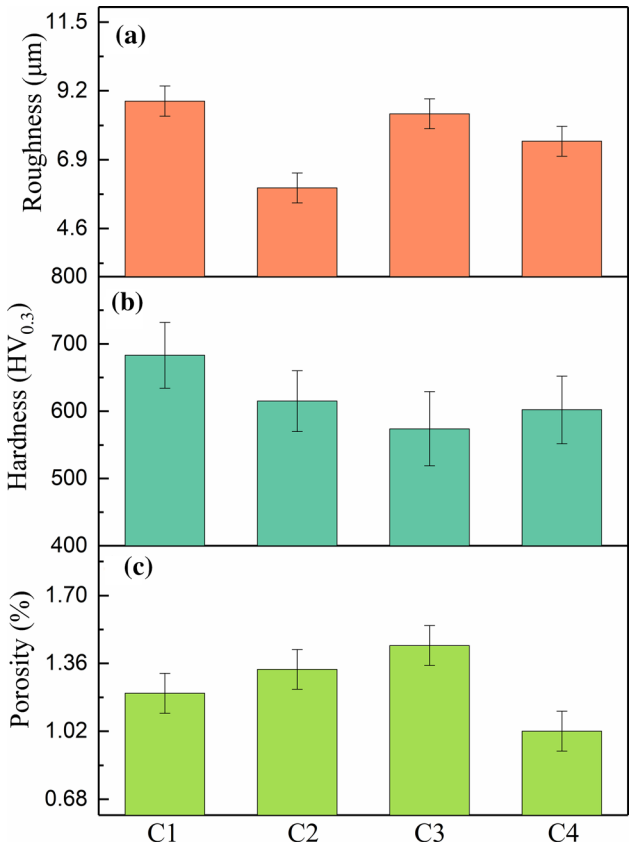

Fig. 9 The roughness, hardness, and porosity of the coatings

roughness value of 8.86 μm due to the sputtering phenomenon of the fine powder P1. C3 showed a similar high value of roughness due to fragmented splats caused by reducing the deformation of the large particles (Fig. 7c2). C2 presented the lowest roughness value, which also reflected a sufficient melting state of the particles during the dynamic deposition process.

In general, tribological properties are determined by many factors. For example, the applied load, sliding speed, test temperature, and atmospheric environment significantly affect the wear resistance. As such, the sliding velocity was set to 0.1 and 0.2 m/s. Figure 10 depicts the wear rates, coefficient of friction (COF), hardness (*H*), elastic modulus (*E*), and *H/E* of the Al-based quasicrystal coatings. The wear rates were in the range of 0.76×10^{-4}–15.80×10^{-4} mm^3/Nm, while the COFs were in the range of 0.44–0.55, which were calculated in the steady-state periods. A comparison of the C1 and C2 coatings without unmelted particles indicated that C1 possessed the lower wear rate under the two applied sliding speeds due to a more uniform microstructure and higher hardness. Thus, triggering spalling of the coating was difficult during the wear process. However, the wear rates of C1 were sensitive to the sliding speed, such that the value of the wear rate for C1 doubled when the sliding speed increased. More severe oxidation phenomenon was observed at the layer interface. Meanwhile, due to the relatively low hardness and high porosity, the wear rate of C3 increased up to 1.58×10^{-3} mm^3/Nm when tested at 0.1 m/s. A further increase in the friction speed destroyed the integrity of C3 during the friction process. The inherent brittleness of the quasicrystalline coatings, which behave as ceramic materials at room temperature, induced cracks when the applied loads and/or velocity were sufficiently high, thereby severely compromising the wear resistance. Figure 10(c) shows the hardness (*H*), elastic modulus (*E*), and their ratio (*H/E*) of the Al-Cu-Fe-Cr coatings. The results show that *H*, *E*, and *H/E* of the Al-Cu-Fe-Cr coatings were in the ranges of 5.5–6.7 GPa, 150.6–165.7 GPa, and 0.037–0.041 GPa, respectively, while the *H/E* ratio evolved in a way similar to that for the wear resistance. The high hardness provided sufficient load support, while the low elastic modulus contributed to the improved fracture toughness when the coatings tested under abrasion, impact, and erosive conditions. Thus, a high *H/E* value represents, on the one hand, the high resistance of a material to plastic deformation, and, on the other hand, retarded crack initiation and propagation caused by cyclic shear stress (Ref 23, 24). In addition, the low surface adhesion energy of the quasicrystals also helped reduce the adhesive contribution to the COF values during the wear test (Ref 2). As a result, the hard Al-Cu-Fe-Cr coatings, which were still ductile, showed a high wear resistance in comparison to the wear-resistant aluminum alloys.

The profile of the wear track is shown in Fig. 11. The wear width and depth, which acted as an indicator of the wear resistance, first showed an upward trend and then rapidly decreased at the two sliding velocities. C1 possessed the smallest width and depth values under the two sliding speeds, indicating the best wear resistance. Additionally, as the sliding speed increased, the value of width and depth of C1 increased from 650.5 μm and 28.5 to 800.7 μm and 51.8 μm. Therefore, these two parameters indicated that the wear resistance was highly sensitive to the sliding velocity.

Phenomena Characteristic of the Particle Impact onto the Plane Solid Surfaces

A HVAF-sprayed coating is formed through mechanical interlocking or physical adhesion of massive in-flight droplets with a substrate. To observe the impact behavior of the droplet during deposition process, single splats deposited with P1, P2, P3, and P5 were observed to understand the droplet spreading behavior upon impact to the substrate. As shown in Fig. 12, the splats can be divided into following types based on their morphologies: partially melted splat, splash splat, flower splat, near disk-

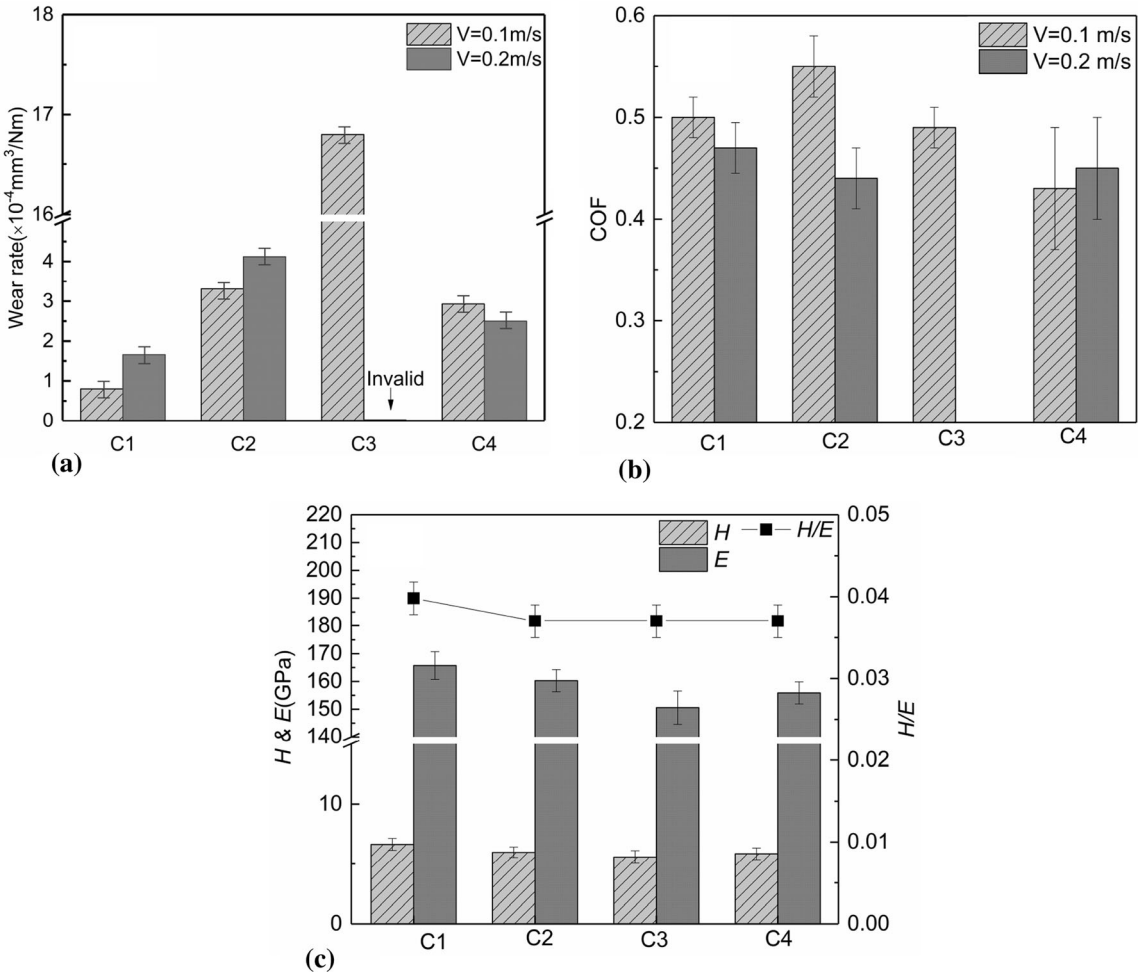

Fig. 10 Wear rates (a), coefficient of friction (b), hardness (*H*), elastic modulus (*E*) and *H/E* ratio (c) of Al-based quasicrystal coatings

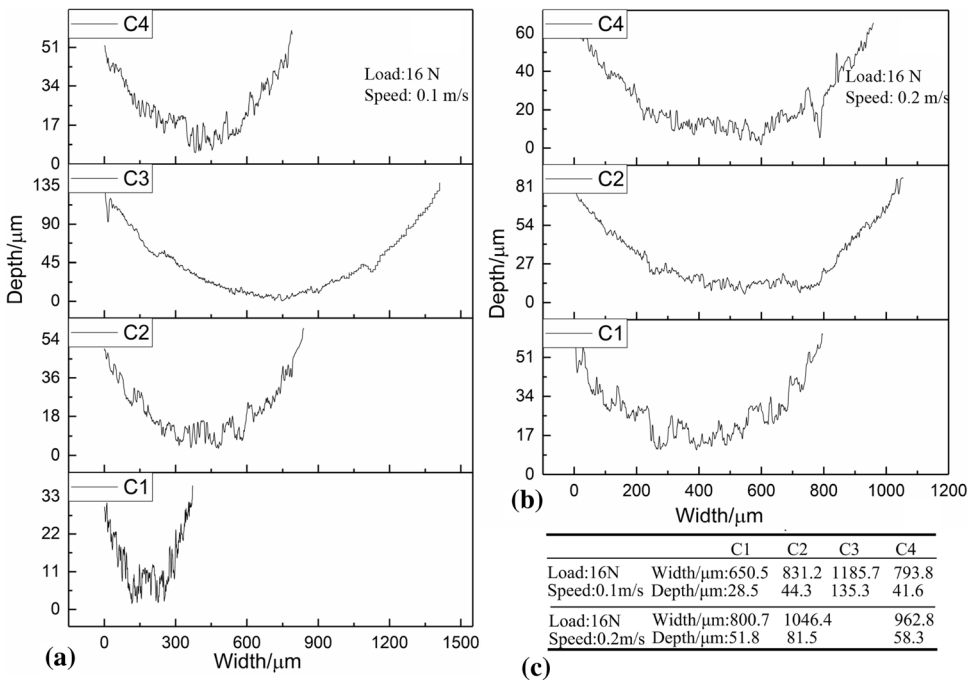

		C1	C2	C3	C4
Load:16N Speed:0.1m/s	Width/μm:650.5 Depth/μm:28.5	831.2 44.3	1185.7 135.3	793.8 41.6	
Load:16N Speed:0.2m/s	Width/μm:800.7 Depth/μm:51.8	1046.4 81.5		962.8 58.3	

Fig. 11 Sectional profiles of the wear tracks of QC coatings tested at different conditions: (a) Load 16 N, sliding speed 0.1 m/s, (b) load 16 N, sliding speed 0.2 m/s

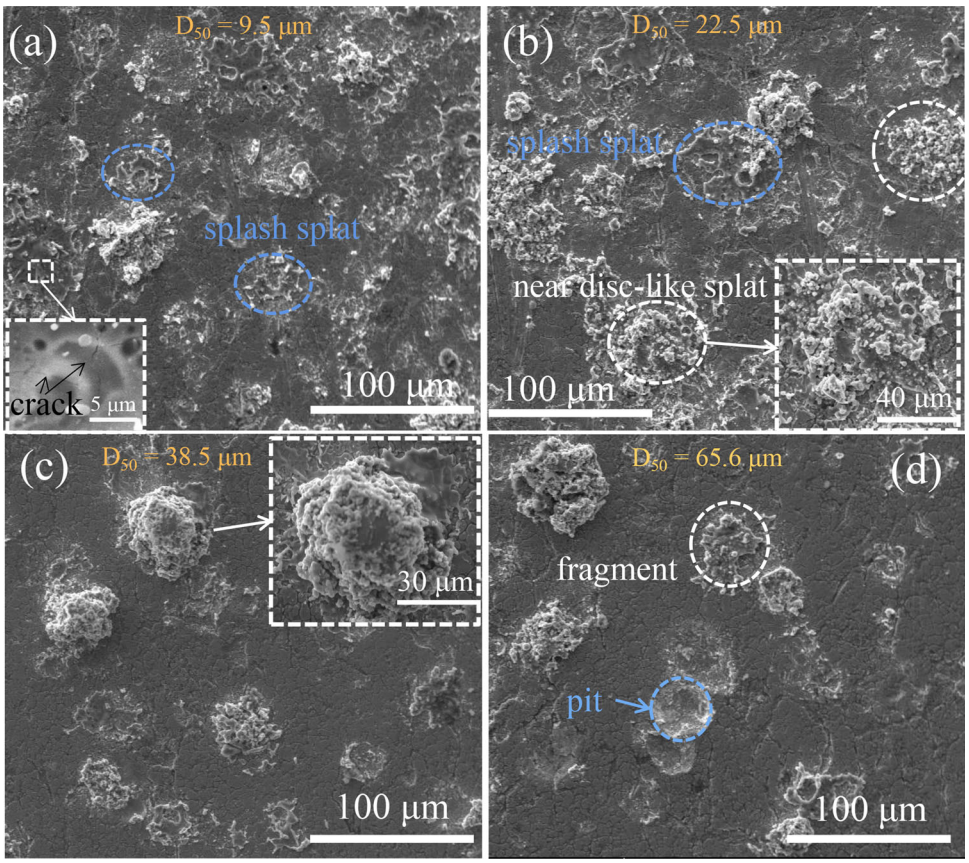

Fig. 12 Morphologies of the splats of QC powders with different particle sizes: (a) P1, (b) P2, (c)P3, and (d) P5

like splat, and ring splat. According to Fig. 12(a), the splash splats or flower-like splat were formed, and several cracks and pores were observed on the smooth surface of the flower-like splat. The crack was caused by the thermal stress and the pore originated from the gas absorbed during the collision between the droplet and substrate. In addition, fine droplets with high velocity were observed with noticeable sputtering when impacting onto substrate. As a result, C1 showed the lowest deposition efficiency. As the powder size increased, the near disk-like splat together with splash splats was observed (Fig. 12b). Fragments were embedded in the re-solidified droplet, revealing the melting state of the droplet was in the solid–liquid two-phase state. However, when the particle size further increased, the melting state rapidly decreased. Figure 12(c) shows the partially melted particles with little smooth splat located at the bottom of the particle, indicating that the energy gained from the flame was not high enough to heat and accelerate powder deformation. When these partially melted splat and fragmented splats were stacked against each other, pores formed more easily and thus generated a loose microstructure. A further increase in the particle size produced several deep pits on the substrate, as shown in Fig. 12(d). The erosion pits revealed that the corresponding particles were in the unmelted state. During the deposition process, these unmelted particles may have eroded the formed deposited splats, thus decreasing the deposition efficiency. As a result, C3 showed a lower thickness per pass as compared to that of C2. However, the large particles also showed a strong peening effect on the already deformed splats during the dynamic spraying process, such that C4 contained unmelted particles that, however, possessed the lowest porosity. Based on the morphology variation (Fig. 12) and the coating deposition efficiency (Fig. 8), it can be concluded that as the particle size increased the particle impact behavior initially transformed from "adhesion + sputtering" to "adhesion" and eventually changed into "rebound +abrasion".

Tribological Morphologies and Wear Mechanisms

Figure 13 presents the morphologies of the wear track and the EDS mapping, which were performed to investigate the wear behavior of the Al-based QC coatings. The worn surfaces present a white-contrast zone and a dark-contrast zone. The white-contrast zone (point 1) was almost consistent with the nominal composition, and the dark-contrast zone (point 2) corresponded to highly oxidized worn-off debris. For the sliding friction of C1 at 0.1 and 0.2 m/s, the

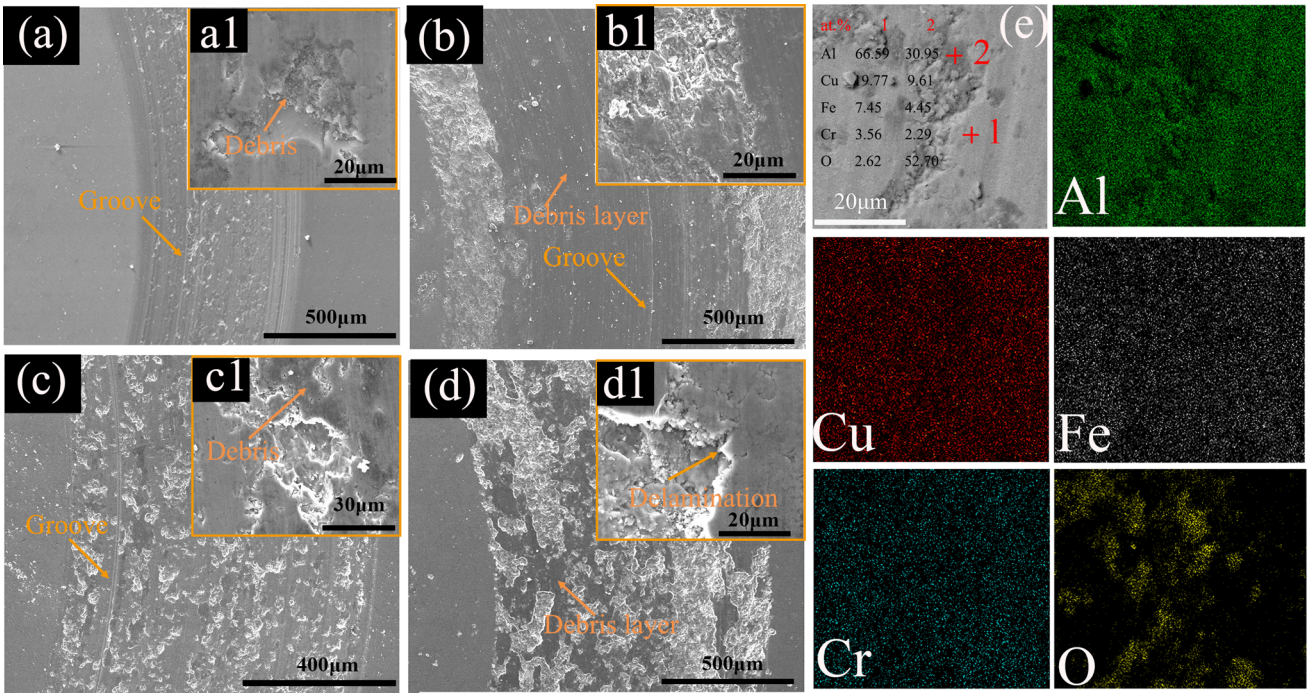

Fig. 13 Worn surface of QC coatings tested at different sliding velocity and EDS mapping: (a) C1,0.1 m/s, (b) C3,0.1 m/s, (c) C1,0.2 m/s, (d) C2,0.2 m/s, (e) EDS mapping of C4

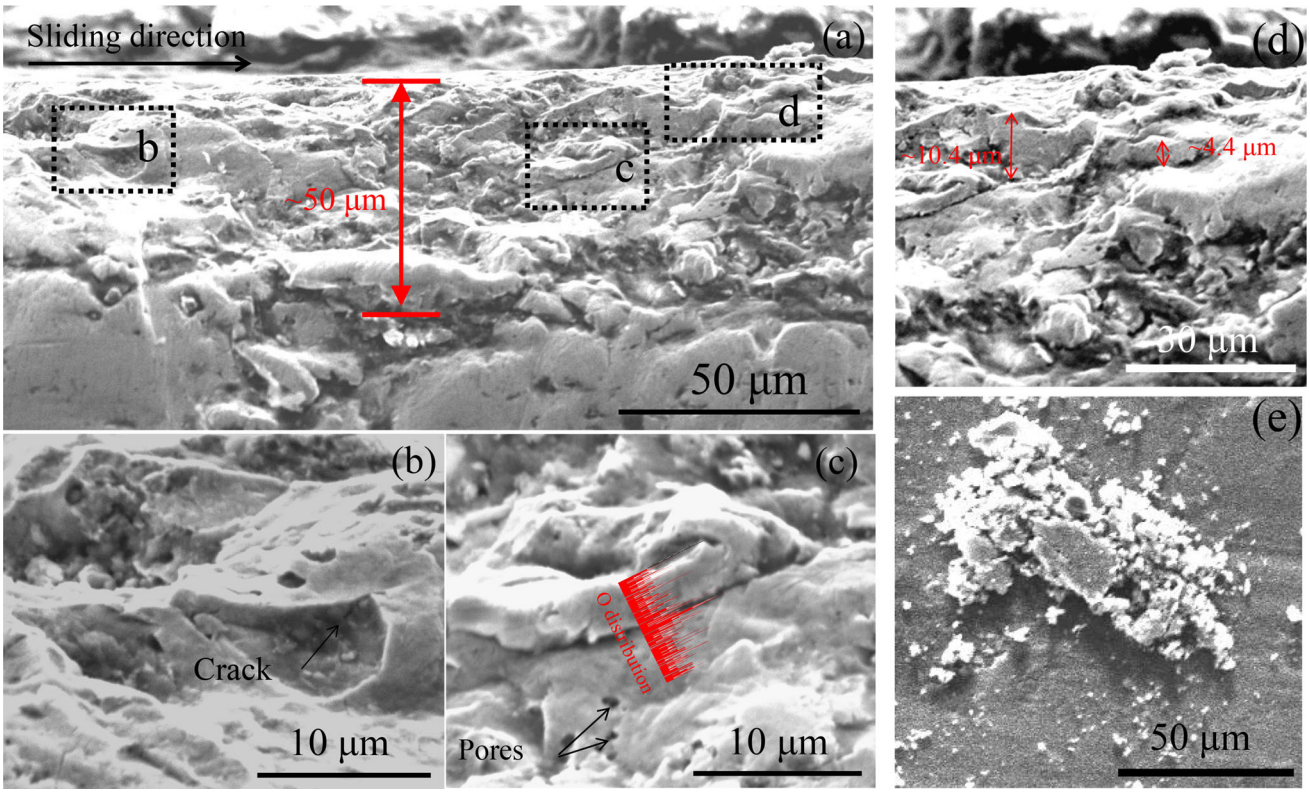

Fig. 14 SEM micrograph of the wear track cross section of coating C2: (a) A whole view; (b), (c) and (d) magnified view of selected area from (a); (e) wear debris

typical plowing grooves and pits in Fig. 13(a) and (c) revealed the appearance of abrasive wear. For the sliding friction of C3 at 0.1 m/s and C2 at 0.2 m/s, delamination is observed in Fig. 13(b) and (d). The C2 coating tested at 0.2 m/s suffered more severe delamination wear, such that a large amount of fine wear debris detached from the matrix and then partially adhered on the wear track. For the Al-based QC coatings, a looser microstructure and higher sliding velocity resulted in crack initiation at the defect sites. These regions, filled with pores and loose oxidation area, accelerated the growth and propagation of the microcracks. After the cracks grew to a critical length, the peeling process was easily trigged and finished at a short time under the combining effect of the vertical load and tangential load. Finally, although most of the debris was removed from the worn track under the shear stress, partially retained debris was smeared and pressed into the debris layer form, as shown in Fig. 13(b) and (d). As compared to the continuous debris layer of C3 tested at 0.1 m/s (Fig. 13b), the morphology of debris layer of C2 exhibited a plateau (Fig. 13d). These findings were a result of layer burst due to brittleness or built up of residual stress after the thickness of oxide layer reached its maximum with continued sliding friction.

In general, the wear behavior of the coatings depended on both the surface and subsurface. Therefore, the cross sections of the coating after wear testing were also examined. Figure 14 shows the SEM micrograph of cross-sectional wear track of the C2coating under an applied load of 16 N and a sliding speed of 0.1 m/s. As observed in Fig. 6(a), the average wear depth was approximately 50 μm, which was consistent with the result obtained from sectional profiles in Fig. 10(a). Some small cracks propagated within the splat (Fig. 14b) and big cracks running along the intersplat regions (Fig. 14c) were observed on the cross-sectional image. Additionally, some pores were also detected on the fracture surface, and the intensity of O reached its peak value at the interface region. These defects sites may have promoted the generation and propagation of the cracks when cyclic shear stress was transmitted from the contact surface area, thus further resulting in its delamination. Figure 14(d) indicates that the height of the fracture surface was approximately in the range of 4.4–10.4 μm, which was larger than that of the worn-off debris (Fig. 14e), revealing that the debris produced in this case experienced a cyclic grinding process. The SEM/EDX analyses (Fig. 13 and 14) on the worn surface and subsurface revealed that the dominating wear mechanism of the Al-based QC coatings in air was initially abrasive wear, which then turned into delamination, abrasive wear, and intensified oxidative wear.

Conclusions

In this work, the effects of the particle size on the mechanical properties of HVAF-sprayed Al-based QC coatings and splats morphology were investigated in detail. Based on the results, the following conclusions can be derived.

1. The particle size significantly affected the coating properties. The coatings sprayed with the finest powders showed a better wear resistance. In addition, the most severe oxidation and Al loss was observed during spraying. In comparison, the wear rate of the coating prepared by coarser powders exhibited less sensitivity to the sliding velocity. The most compact structure was obtained for powders with the widest size range of +12 μm–49 μm.
2. An increase in the particle size helped maintain the quasicrystalline content of the coatings, which reached the maximum volume fraction of 29.0% in the HVAF-sprayed Al-based QC coating.
3. An increase in the particle size led to the impact behavior of the droplets onto the substrate surface transformed from "adhesion + sputtering" to "adhesion" and finally to "rebound + abrasion".
4. The friction coefficient and wear rate of the QC coatings were approximately 0.45 and 7.6×10^{-5} mm^3/Nm, respectively. The high hardness and dense microstructure were responsible for the good wear resistance. With continuous wear, the dominant wear mechanisms transferred from abrasive wear to delamination, abrasive wear, and intensified oxidative wear.

Acknowledgments This work was supported by the National Natural Science Foundation of China (Grant No. 51901079), the Fundamental Research Funds for the Central Universities, the Opening Project of National Engineering Research Center for Powder Metallurgy of Titanium and Rare Metals, the Natural Science Foundation of Guangdong Province (Nos. 2018A030313615, 2018A030310406, 2020A1515010736), the Guangzhou Municipal Science and Technology Program (No. 202007020008), the Zhongshan Municipal Science and Technology Program (2019010408) and Zhongshan Collaborative Innovation Fund (2018C1001). In addition, we thank LetPub (www.letpub.com) for its linguistic assistance during the preparation of this manuscript.

References

1. C. Zhou, R. Cai, S. Gong, and H. Xu, Hot Corrosion of AlCuFeCr Quasicrystalline Coating on Titanium Alloys with NaCl Deposit, *Surf. Coat. Technol.*, 2006, **201**(3-4), p 1718-1723
2. W. Wolf, G.Y. Koga, R. Schulz, S. Savoie, C.S. Kiminami, C. Bolfarini, and W.J. Botta, Wear and Corrosion Performance of

Al-Cu-Fe-(Cr) Quasicrystalline Coatings Produced by HVOF, *J. Therm. Spray Technol.*, 2020, **29**, p 1195-1207
3. W. Wolf, R. Schulz, S. Savoie, C. Bolfarini, C.S. Kiminami, and W.J. Botta, Structural, Mechanical and Thermal Characterization of an Al-Co-Fe-Cr Alloy for Wear and Thermal Barrier Coating Applications, *Surf. Coat. Technol.*, 2017, **319**, p 241-248
4. T. Moskalewicz, B. Dubiel, and B. Wendler, AlCuFe(Cr) and AlCoFeCr Coatings for Improvement of Elevated Temperature Oxidation Resistance of a Near-α Titanium Alloy, *Mater. Charact.*, 2013, **83**, p 161-169
5. E. Fleury, S.M. Lee, W.T. Kim, and D.H. Kim, Effects of Air Plasma Spraying Parameters on the Al–Cu–Fe Quasicrystalline Coating Layer, *J. Non-Cryst. Solids*, 2000, **278**(1), p 194-204
6. V. Matikainen, G. Bolelli, H. Koivuluoto, P. Sassatelli, L. Lusvarghi, and P. Vuoristo, Sliding Wear Behaviour of HVOF and HVAF Sprayed Cr3C2-Based Coatings, *Wear*, 2017, **388-389**, p 57-71
7. V. Matikainen, H. Koivuluoto, and P. Vuoristo, A Study of Cr3C2-based HVOF- and HVAF-Sprayed Coatings: Abrasion, Dry Particle Erosion and Cavitation Erosion Resistance, *Wear*, 2020, **446–447**,
8. D.J. Sordelet, M.F. Besser, and I.E. Anderson, Particle Size Effects on Chemistry and Structure of Al-Cu-Fe Quasicrystalline Coatings, *J. Therm. Spray Technol.*, 1996, **5**(2), p 161-174
9. Y. Bai, L. Zhao, Y. Wang, D. Chen, B.Q. Li, and Z.H. Han, Fragmentation of In-Flight Particles and Its Influence on the Microstructure and Mechanical Property of YSZ Coating Deposited by Supersonic Atmospheric Plasma Spraying, *J. Alloys Compd.*, 2015, **632**, p 794-799
10. C.J. Li and Y.Y. Wang, Effect of Particle State on the Adhesive Strength of HVOF Sprayed Metallic Coating, *J. Therm. Spray Technol.*, 2002, **11**(4), p 523-529
11. Z. Yin, S. Tao, X. Zhou, and C. Ding, Particle In-Flight Behavior and Its Influence on the Microstructure and Mechanical Properties of Plasma-Sprayed Al_2O_3 Coatings, *J. Eur. Ceram. Soc.*, 2008, **28**(6), p 1143-1148
12. L. Zhao, K. Seemann, A. Fischer, and E. Lugscheider, Study on Atmospheric Plasma Spraying of Al2O3 Using On-Line Particle Monitoring, *Surf. Coat. Technol.*, 2003, **168**(2–3), p 186-190
13. G. Ma, S. Chen, P. He, H. Wang, Y. Zhou, Q. Zhao, and G. Li, Particle In-Flight Status and Its Influence on the Properties of Supersonic Plasma-Sprayed Fe-Based Amorphous Metallic Coatings, *Surf. Coat. Technol.*, 2019, **358**, p 394-403
14. A. Ünal, Liquid Break-Up in Gas Atomization of Fine Aluminum Powders, *Metall. Trans. B*, 1989, **20**(1), p 61-69
15. N. Zeoli and S. Gu, Computational Simulation of Metal Droplet Break-Up, Cooling and Solidification During Gas Atomisation, *Comput. Mater. Sci.*, 2008, **43**(2), p 268-278
16. R.S. Maurya, A. Sahu, and T. Laha, Quantitative Phase Analysis in Al86Ni8Y6 Bulk Glassy Alloy Synthesized by Consolidating Mechanically Alloyed Amorphous Powder Via Spark Plasma Sintering, *Mater. Des.*, 2016, **93**, p 96-103
17. W. Tillmann, O. Khalil, and I. Baumann, Influence of Spray Gun Parameters on Inflight Particle's Characteristics, the Splat-Type Distribution, and Microstructure of Plasma-Sprayed YSZ Coatings, *Surf. Coat. Technol.*, 2021, **406**, p 126705-126717
18. A. Kumar, S.K. Nayak, K. Sarkar, A. Banerjee, K. Mondal, and T. Laha, Investigation of Nano- and Micro-Scale Structural Evolution and Resulting Corrosion Resistance in Plasma Sprayed Fe-Based (Fe-Cr-B-C-P) Amorphous Coatings, *Surf. Coat. Technol.*, 2020, **397**, p 126058-126059
19. A. Zakeri, E. Bahmani, and A.S.R. Aghdam, Impact of MCrAlY Feedstock Powder Modification by High-Energy Ball Milling on the Microstructure and High-Temperature Oxidation Performance of HVOF-Sprayed Coatings, *Surf. Coat. Technol.*, 2020, **395**, p 125935-125947
20. T. Fedina, J. Sundqvist, J. Powell, and A.F.H. Kaplan, A Comparative Study of Water and Gas Atomized Low Alloy Steel Powders for Additive Manufacturing, *Addit. Manuf.*, 2020, **36**, p 101675-101686
21. X.B. Zhao and Z.H. Ye, Microstructure and Wear Resistance of Molybdenum Based Amorphous Nanocrystalline Alloy Coating Fabricated by Atmospheric Plasma Spraying, *Surf. Coat. Technol.*, 2013, **228**, p S266-S270
22. D. Liang, J. Ma, Y. Cai, X. Liu, S. Xie, X. Wei, G. Xu, and J. Shen, Characterization and Elevated-Temperature Tribological Performance of AC–HVAF-Sprayed Fe-Based Amorphous Coating, *Surf. Coat. Technol.*, 2020, **387**, p 125535-125545
23. J. Guo, H. Wang, F. Meng, X. Liu, and F. Huang, Tuning the H/E* ratio and E* of AlN Coatings by Copper Addition, *Surf. Coat. Technol.*, 2013, **228**, p 68-75
24. J. Musil, Hard Nanocomposite Coatings: Thermal Stability, Oxidation Resistance and Toughness, *Surf. Coat. Technol.*, 2012, **207**, p 50-65